Electronic Supplementary Material (ESI) for Dalton Transactions.
This journal is © The Royal Society of Chemistry 2021

Effect of Ligand Substituent and Tuning the Spin-State Switching in Manganese(III) Complexes

*Subrata Ghosh, Sukanya Bagchi, Sujit Kamilya and Abhishake Mondal**[†]

[†]*Solid State and Structural Chemistry Unit, Indian Institute of Science, Sir C V Raman Road, Bangalore 560012, India*

Email: mondal@iisc.ac.in

Table of Content:

Experimental Section 5

Materials and physical measurements 5

Magnetic Measurements 5

X-ray crystallography 6

Figures 7

Tables 30

References 37

Figure S1. Picture of crystals for complexes **1 – 3** (left to right). 7

Figure S2. Comparison of the room temperature experimental PXRD pattern and the 240 K simulated one for **1**. 7

Figure S3. Comparison of the room temperature experimental PXRD pattern and the 240 K simulated one for **2**. 7

Figure S4. Comparison of the room temperature experimental PXRD pattern and the 240 K simulated one for **3**. 8

Figure S5. TGA curves for **1 – 3** from 303 K to 573 K temperature range at 10 K min^{-1} sweep rate under N_2 atmosphere. 8

Figure S6. ATR IR spectra of **1** – **3** at room temperature. 9

Figure S7. Perspective view of unit cell in **1** at 240 K. Hydrogen atoms are omitted for clarity (Mn: Purple, C: gray, N: blue, O: red, B: light-pink). 9

Figure S8. Perspective view of unit cell in **2** at 240 K. Hydrogen atoms are omitted for clarity (Mn: Purple, C: gray, N: blue, O: red, Br: brown, B: light-pink). 10

Figure S9. Perspective view of unit cell in **3** at 240 K. Hydrogen atoms are omitted for clarity (Mn: Purple, C: gray, N: blue, O: red, Br: brown, B: light-pink). 10

Figure S10. Perspective view of unit cell packing along the *a*-axis in **2** at 240 K. Counter-anions and hydrogen atoms are omitted for clarity (Mn(HS), red, polyhedral environment). 11

Figure S11. Perspective view of unit cell in **2** at 120 K. Hydrogen atoms are omitted for clarity (Mn: Purple, C: gray, N: blue, O: red, Br: brown, B: light-pink). 11

Figure S12. Perspective view of unit cell packing along the *a*-axis in **2** at 120 K. Counter-anions and hydrogen atoms are omitted for clarity (Mn(intermediate state): violet, polyhedral environment). 12

Figure S13. Perspective view of unit cell in **2** at 100 K. Hydrogen atoms are omitted for clarity (Mn: Purple, C: gray, N: blue, O: red, Br: brown, B: light-pink). 12

Figure S14. Perspective view of unit cell packing along the *a*-axis in **2** at 100 K. Counter-anions and hydrogen atoms are omitted for clarity (Mn(LS): blue, polyhedral environment). 13

Figure S15. Top: Perspective view of a fragment of the supramolecular structure displaying several weak interactions (red lines) in **1** at 240 K. Bottom: View of N–H···C interactions forming 1D chain in **1** at 240 K. 14

Figure S16. Top: Perspective view of a fragment of the supramolecular structure displaying several weak interactions (red lines) in **2** at 240 K. Bottom: View of N–H···C interactions forming 1D chain in **2** at 240 K. 15

Figure S17. Top: Perspective view of a fragment of the supramolecular structure displaying several weak interactions (red lines) in **2** at 120 K. 15

Figure S18. Perspective view of a fragment of the supramolecular structure displaying several weak interactions (red lines) in **2** at 100 K. Bottom: View of N–H···C interactions forming 1D chain in **2** at 100 K. 16

Figure S19. Top: Perspective view of a fragment of the supramolecular structure displaying several weak interactions (red lines) in **3** at 240 K. Bottom: View of N–H···C interactions forming 1D chain in **3** at 240 K. 17

Figure S20. UV-vis-NIR spectra of **1** – **3** in MeCN with dilute (left) and concentrated (right) solutions at room temperature. 17

Figure S21. Solid state UV-vis-NIR spectra of **1** – **3** in KBr at room temperature. 18

Figure S22. DSC plot of **2** shown between 180 and 140 K at a sweep rate of 5 K min^{-1}. 18

Figure S23. Field dependence of the magnetization as *M vs H* plots for **1** (Top, left), **2** (top, right) and **3** (bottom) at 100 K. The solid line is the best fit. 19

Figure S24. Temperature dependence of χT product in log scale for **1** – **3** at 10000 Oe. 19

Figure S25. The first derivative of χT against the temperature, dχT /dT *vs*. T, identifies $T_{1/2}$ (1) = 164 K and $T_{1/2}$ (2) = 98 K for **2**. 20

Figure S26. The first derivative of χT against the temperature, dχT /dT *vs*. T, identifies $T_{1/2}$ (1) = 86 K for **3**. 20

Figure S27. Temperature dependence of χT product for **2** at 10000 Oe in cooling and heating mode. 21

Figure S28. Left: Temperature dependence of χT product for **3** at 10000 Oe in cooling and heating mode. Right: shown selected region (60 - 120K). 21

Figure S29. Field dependence of the magnetization as *M* vs *H* (left) and *M* vs *H/T* (right) plots for **1** at 4 and 8 K. The solid lines are guide for the eyes. 22

Figure S30. Field dependence of the magnetization as *M* vs *H* (left) and *M* vs *H/T* (right) plots for **2** at 4 and 6 K. The solid lines are guide for the eyes. 22

Figure S31. Field dependence of the magnetization as *M* vs *H* (left) and *M* vs *H/T* (right) plots for **3** at 4 and 8 K. The solid lines are guide for the eyes. 22

Figure S32. Cyclic voltammograms for oxidation of **1** – **3** in 0.2 M (^{n}Bu$_4$N)PF$_6$ / MeCN with a scan rate of 100 mV s^{-1}. Arrow indicates the open circuit potential with the direction of the potential sweep. 23

Figure S33. Cyclic voltammograms for reduction of **1** in 0.2 M (^{n}Bu$_4$N)PF$_6$ / MeCN with different scan rate. Arrow indicates the open circuit potential with the direction of the potential sweep. 23

Figure S34. Cyclic voltammograms for oxidation of **1** in 0.2 M (^{n}Bu$_4$N)PF$_6$ / MeCN with a scan rate of 100 mV s^{-1}. Arrow indicates the open circuit potential with the direction of the potential sweep. 24

Figure S35. Cyclic voltammograms for oxidation of **1** (-0.3 V to +0.9V) in 0.2 M (^{n}Bu$_4$N)PF$_6$ / MeCN with different scan rate. Arrow indicates the open circuit potential with the direction of the potential sweep. . 24

Figure S36. Square wave voltammograms for **1** in 0.2 M (^{n}Bu$_4$N)PF$_6$ / MeCN. Arrows indicate the open circuit potential with the direction of the potential sweep. 25

Figure S37. Cyclic voltammograms for reduction of **2** in 0.2 M (^{n}Bu$_4$N)PF$_6$ / MeCN with different scan rate. Arrow indicates the open circuit potential with the direction of the potential sweep. 25

Figure S38. Cyclic voltammogram for oxidation of **2** in 0.2 M (^{n}Bu$_4$N)PF$_6$ / MeCN with a scan rate of 100 mV s^{-1}. Arrow indicates the open circuit potential with the direction of the potential sweep. 26

Figure S39. Square wave voltammograms for **2** in 0.2 M (^{n}Bu$_4$N)PF$_6$ / MeCN. Arrow indicates the open circuit potential with the direction of the potential sweep. 26

Figure S40. Cyclic voltammogram for reduction of **3** in 0.2 M (^{n}Bu$_4$N)PF$_6$ / MeCN with different scan rate. Arrow indicates the open circuit potential with the direction of the potential sweep. 27

Figure S41. Cyclic voltammogram for oxidation of **3** in 0.2 M (^{n}Bu$_4$N)PF$_6$ / MeCN with a scan rate of 100 mV s^{-1}. Arrow indicates the open circuit potential with the direction of the potential sweep. 27

Figure S42. Square wave voltammograms for **3** in 0.2 M (^{n}Bu$_4$N)PF$_6$ / MeCN. Arrow indicates the open circuit potential with the direction of the potential sweep. 28

Figure S43. Cyclic voltammogram for oxidation of NaBPh$_4$ in 0.2 M (^{n}Bu$_4$N)PF$_6$ / MeCN with a scan rate of 100 mV s^{-1}. Arrow indicates the open circuit potential with the direction of the potential sweep. 28

Figure S44. Square wave voltammogram for oxidation of NaBPh$_4$ in 0.2 M (^{n}Bu$_4$N)PF$_6$ / MeCN. Arrow indicates the open circuit potential with the direction of the potential sweep. 29

Table S1. X-ray crystallography data for complexes **1** – **3**. 30

Table S2. Selected bond distances (Å) and bond angles (°) in **1 – 3**. 31

Table S3: CShM analysis data for complexes **1** – **3** 32

Table S4. Spin crossover behaviors of [Mn(X-sal$_2$-323)](BPh$_4$) (X = ligand substituent) complexes with associated Mn–N/O bond distances 33

Table S5: Spin crossover behaviors of [Mn(5H-sal$_2$-323)](Y) (Y = counter anion) complexes with associated Mn–N/O bond distances 34

Table S6: Spin crossover behaviors of [Mn(5Br-sal$_2$-323)](Y) (Y = counteranion) complexes with associated Mn–N/O bond distances 35

Table S7: Spin crossover behaviors of [Mn(3,5Br-sal$_2$-323)](Y) (Y = counter anion) complexes with associated Mn–N/O bond distances 36

Experimental Section

Materials and physical measurements

All manipulations were carried out under air unless otherwise stated. Solvents were dried by standard methods and freshly distilled before use. All chemicals were used as purchased from chemical sources without further purification. The crystals of complexes were removed from the mother liquor and dried on filter paper to remove any adhering solvent molecules, prior to measurement. The elemental analyses of C, H and N were performed with Thermo Scientific Flash 2000 Organic Elemental Analyzer. Infrared (IR) spectra were recorded in the range of 4000 – 400 cm^{-1} on Bruker Tensor 27 spectrometer. UV-vis-NIR spectra were carried out in the region of 250 – 2000 nm on a Lambda 750 UV-vis-NIR spectrometer. The UV-vis spectroscopic measurements in solution were performed in quartz cuvettes with path length of 1 cm. Solid-state measurements were carried out by taking 5% sample by weight in KBr. Thermogravimetric analysis (TGA) was done on a Mettler Toledo TGA/SDTA851 analyzer with a heating rate of 10 K min^{-1} under a nitrogen atmosphere ranging from 300 K to 573 K. Differential scanning calorimetry (DSC) measurements were performed using Mettler Toledo DSC 823^e differential scanning calorimeter with a scan rate of 10 K min^{-1} and 5 K min^{-1} in a nitrogen atmosphere. Powder X-ray diffraction (PXRD) measurements were carried out on a PANalytical Empyrean diffractometer at 45 kV and 30 mA, under Cu-Kα radiation (λ = 1.54059 Å). PXRD data analyses were done using PANalytical X'Pert HighScore Plus software.[1] Electrochemistry experiments were performed with a Metrohm Autolab PGSTAT101 using platinum as working electrode in acetonitrile with 0.2 M (^{n}Bu$_4$)NPF$_6$ as supporting electrolyte. Ferrocene was used as an internal reference.

Magnetic Measurements

The magnetic susceptibility measurements were carried out with Quantum Design MPMS-XL EverCool SQUID magnetometer, between 2 and 300 K for dc applied fields ranging from -5 T to 5 T for **1** - **3**. Polycrystalline samples of **1** - **3** (18.58, 20.62 and 13.55 mg, respectively) introduced

in a polyethylene bag (2.8 × 0.75 × 0.02 cm) were subjected to measurements. The temperature dependent data were measured using 1000 Oe, 5000 Oe and 10000 Oe dc fields. The isothermal magnetization data were acquired at 4 and 8 K (for **1** and **3**) and 4 and 6 K (for **2**). *M vs H* measurements were performed at 100 K to check for the presence of ferromagnetic impurities which were found to be absent. The magnetic data were corrected for the sample holder and the diamagnetic contribution.

X-ray crystallography

Single crystal X-ray structure analysis data of the complexes **1 - 3** were collected with a Bruker SMART APEX CCD diffractometer equipped with graphite monochromated MoKα radiation (λ = 0.71073 Å). The single crystals were mounted on crystal mounting loop with the help of Paratone oil at 240 K followed by data collection. The same crystal was slowly cooled down to 120 K and 100 K with 2 K / min ramping rate, followed by data collection. Data integration and reduction were performed with the help of SAINT software, and empirical absorption corrections were applied with SADABS programme.[2] Structures were solved using direct methods and refined with a full-matrix least-squares method on F^2 using SHELXT-2014[3] in WinGX programs suite.[4] All non-hydrogen atoms were refined using anisotropic displacement parameters. Hydrogen atoms were labeled to ideal positions and refined isotropically using a riding model. To handle the atomic position disorder of C atoms in the phenyl ring of BPh_4^- counter anion, C atoms of phenyl rings were refined with a free variable associated with the occupancy. The total sum occupancy for the different parts of the same C atoms was constrained to be 1. Same has been applied for disordered Br atom in all complexes. The PART instruction has been used to constrain the equivalent atomic displacement parameter. Additionally, SIMU restraint has also been used for appropriate carbon atoms with anisotropic refinement in SHELXL-2018. Hydrogen atoms on the disordered phenyl rings were not introduced but are taken into account in the complex formula.

Figures

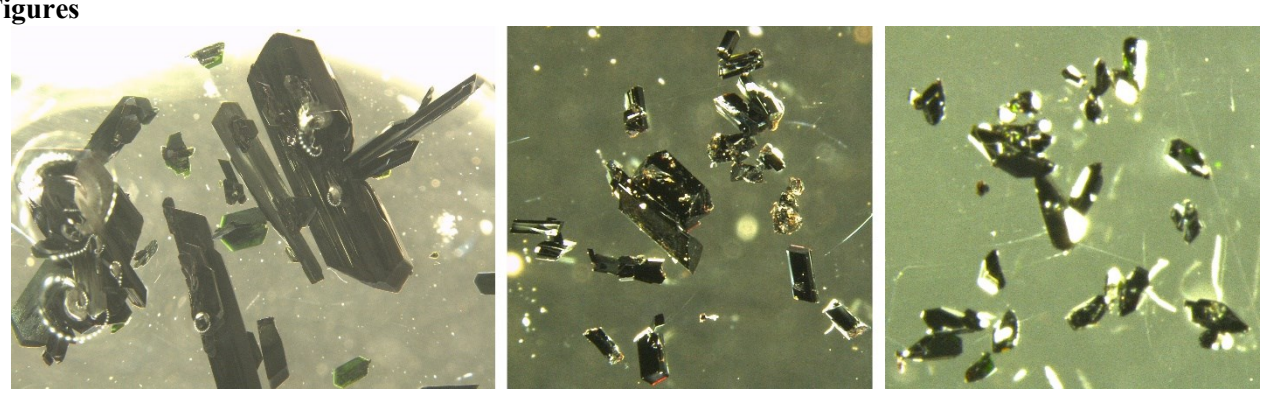

Figure S1. Picture of crystals for complexes **1 – 3** (left to right).

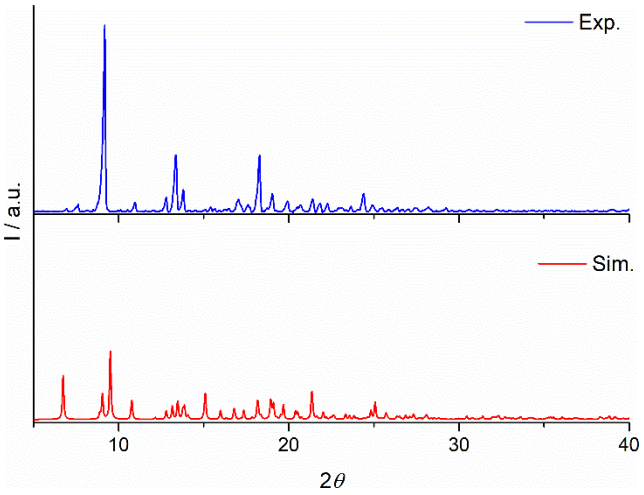

Figure S2. Comparison of the room temperature experimental PXRD pattern and the 240 K simulated one for **1**.

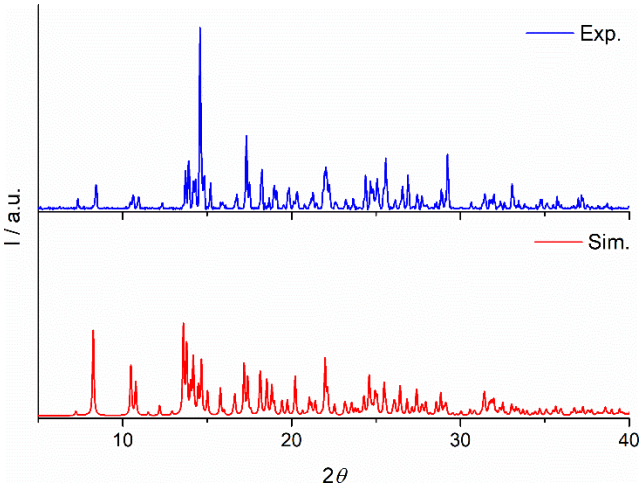

Figure S3. Comparison of the room temperature experimental PXRD pattern and the 240 K simulated one for **2**.

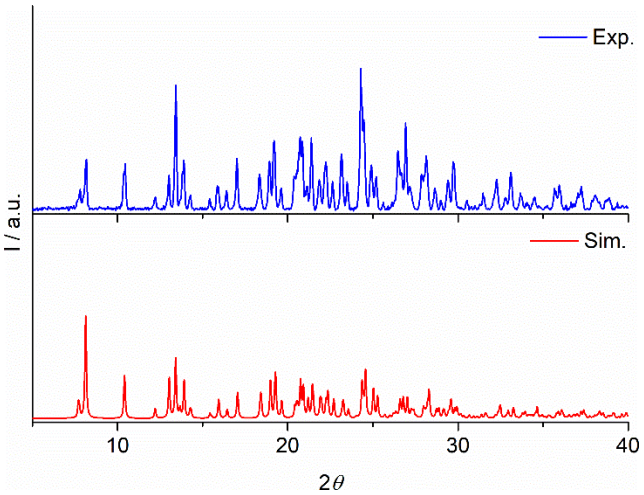

Figure S4. Comparison of the room temperature experimental PXRD pattern and the 240 K simulated one for **3**.

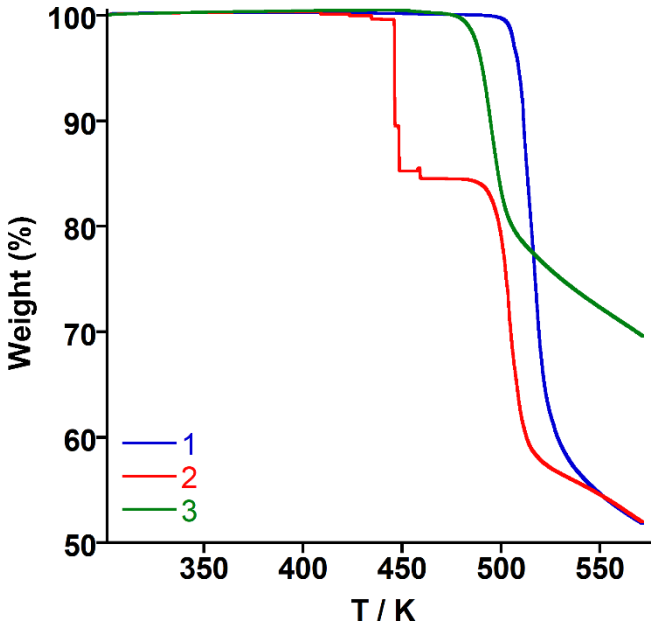

Figure S5. TGA curves for **1 – 3** from 303 K to 573 K temperature range at 10 K min^{-1} sweep rate under N_2 atmosphere.

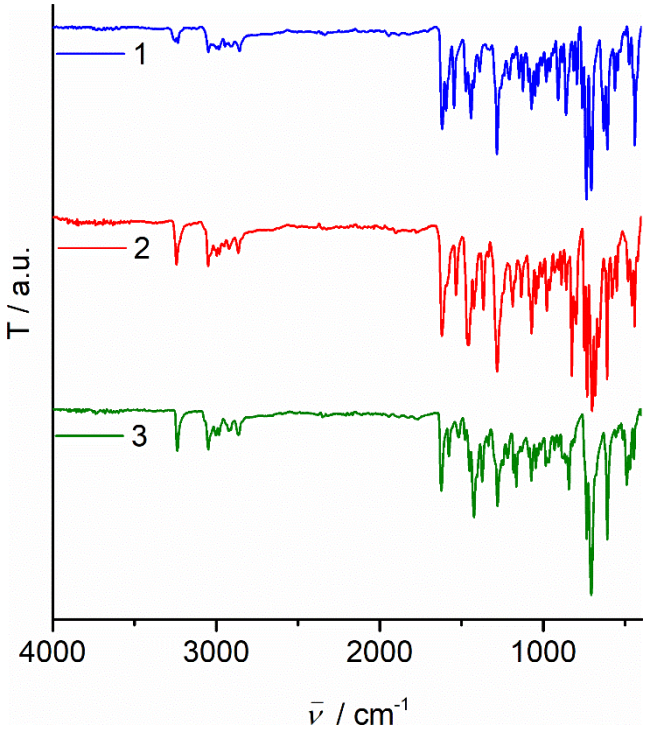

Figure S6. ATR IR spectra of **1** – **3** at room temperature.

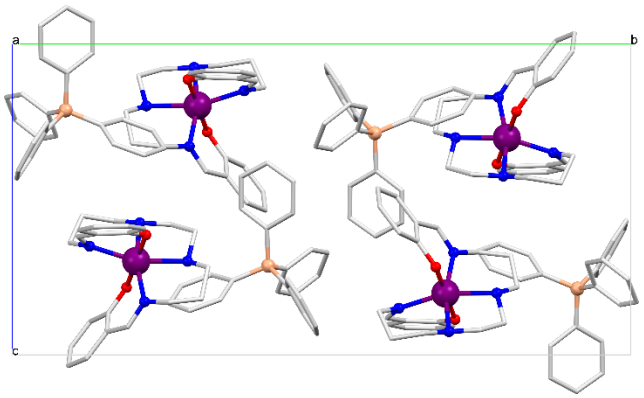

Figure S7. Perspective view of unit cell in **1** at 240 K. Hydrogen atoms are omitted for clarity (Mn: Purple, C: gray, N: blue, O: red, B: light-pink).

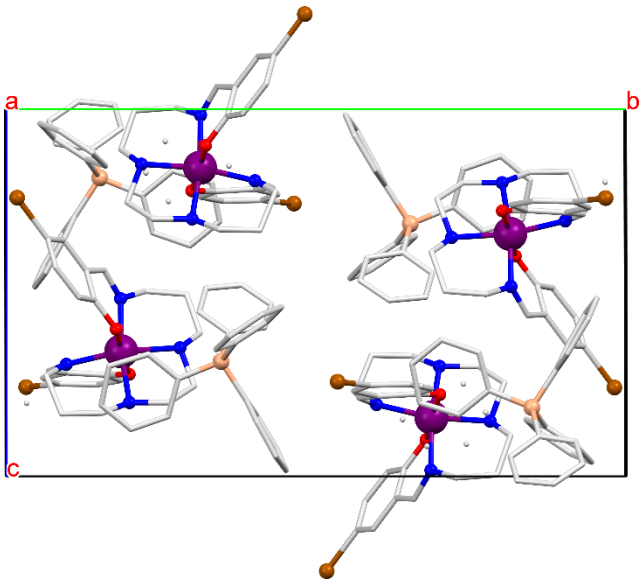

Figure S8. Perspective view of unit cell in **2** at 240 K. Hydrogen atoms are omitted for clarity (Mn: Purple, C: gray, N: blue, O: red, Br: brown, B: light-pink).

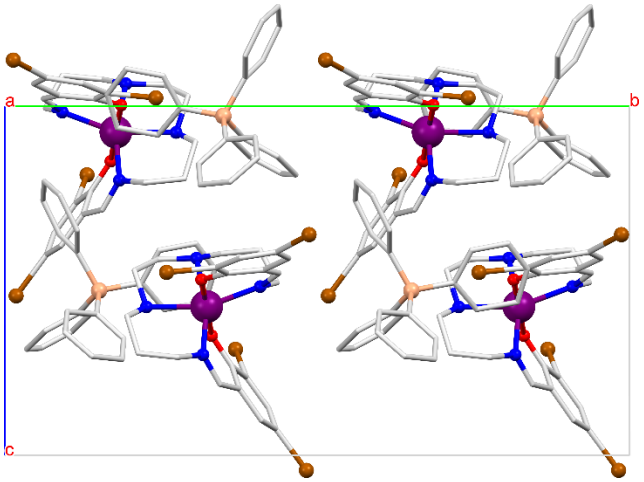

Figure S9. Perspective view of unit cell in **3** at 240 K. Hydrogen atoms are omitted for clarity (Mn: Purple, C: gray, N: blue, O: red, Br: brown, B: light-pink).

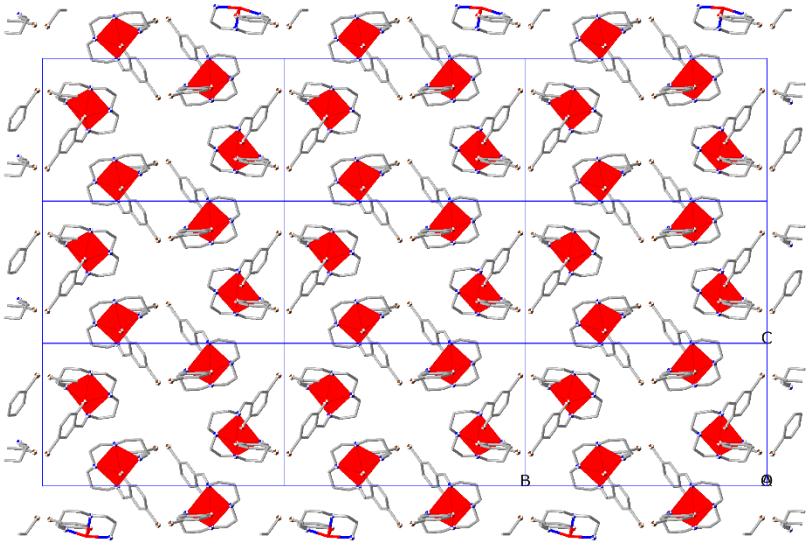

Figure S10. Perspective view of unit cell packing along the *a*-axis in **2** at 240 K. Counter-anions and hydrogen atoms are omitted for clarity (Mn(HS), red, polyhedral environment).

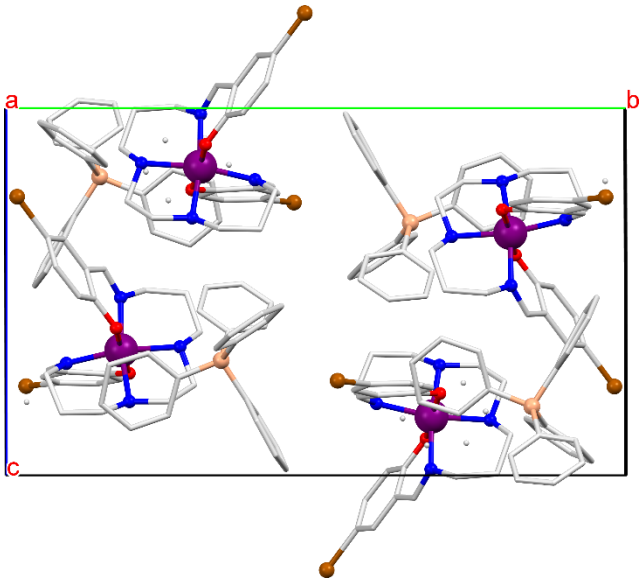

Figure S11. Perspective view of unit cell in **2** at 120 K. Hydrogen atoms are omitted for clarity (Mn: Purple, C: gray, N: blue, O: red, Br: brown, B: light-pink).

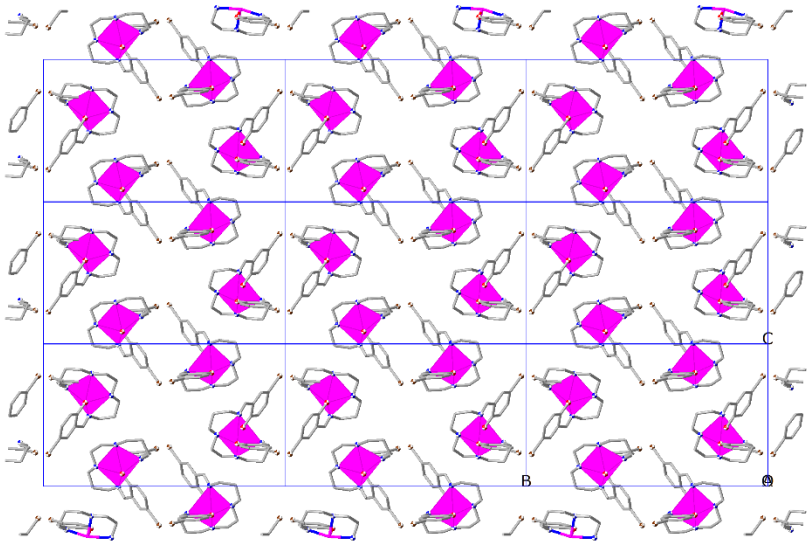

Figure S12. Perspective view of unit cell packing along the *a*-axis in **2** at 120 K. Counter-anions and hydrogen atoms are omitted for clarity (Mn(intermediate state): violet, polyhedral environment).

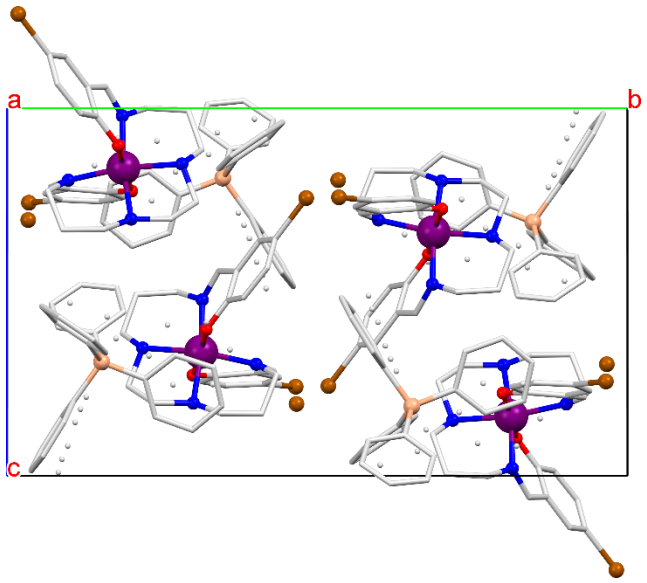

Figure S13. Perspective view of unit cell in **2** at 100 K. Hydrogen atoms are omitted for clarity (Mn: Purple, C: gray, N: blue, O: red, Br: brown, B: light-pink).

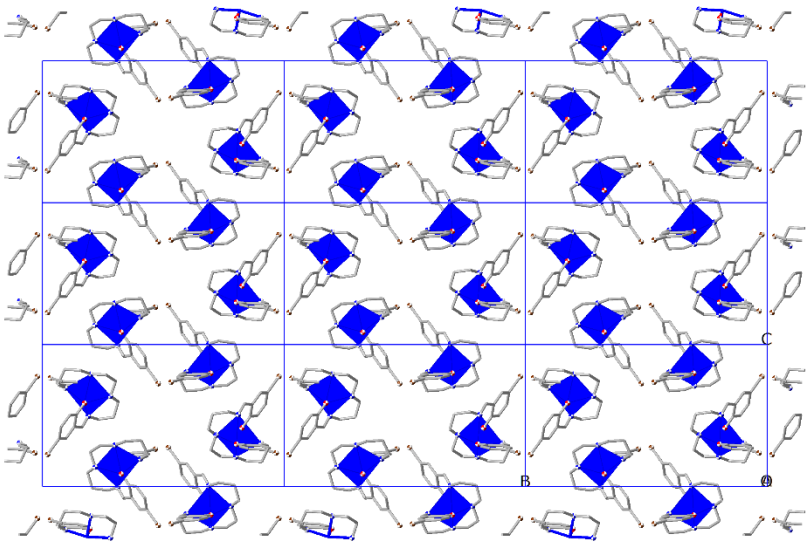

Figure S14. Perspective view of unit cell packing along the *a*-axis in **2** at 100 K. Counter-anions and hydrogen atoms are omitted for clarity (Mn(LS): blue, polyhedral environment).

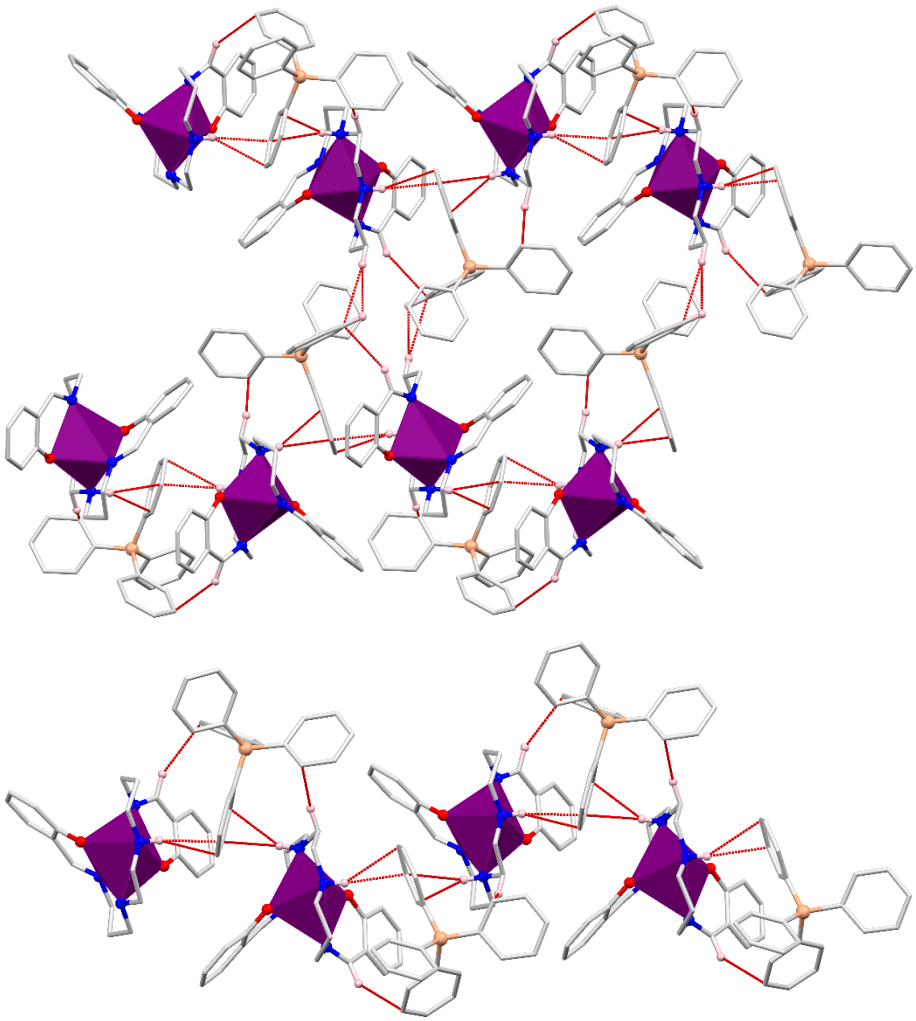

Figure S15. Top: Perspective view of a fragment of the supramolecular structure displaying several weak interactions (red lines) in **1** at 240 K. Bottom: View of N–H···C interactions forming 1D chain in **1** at 240 K.

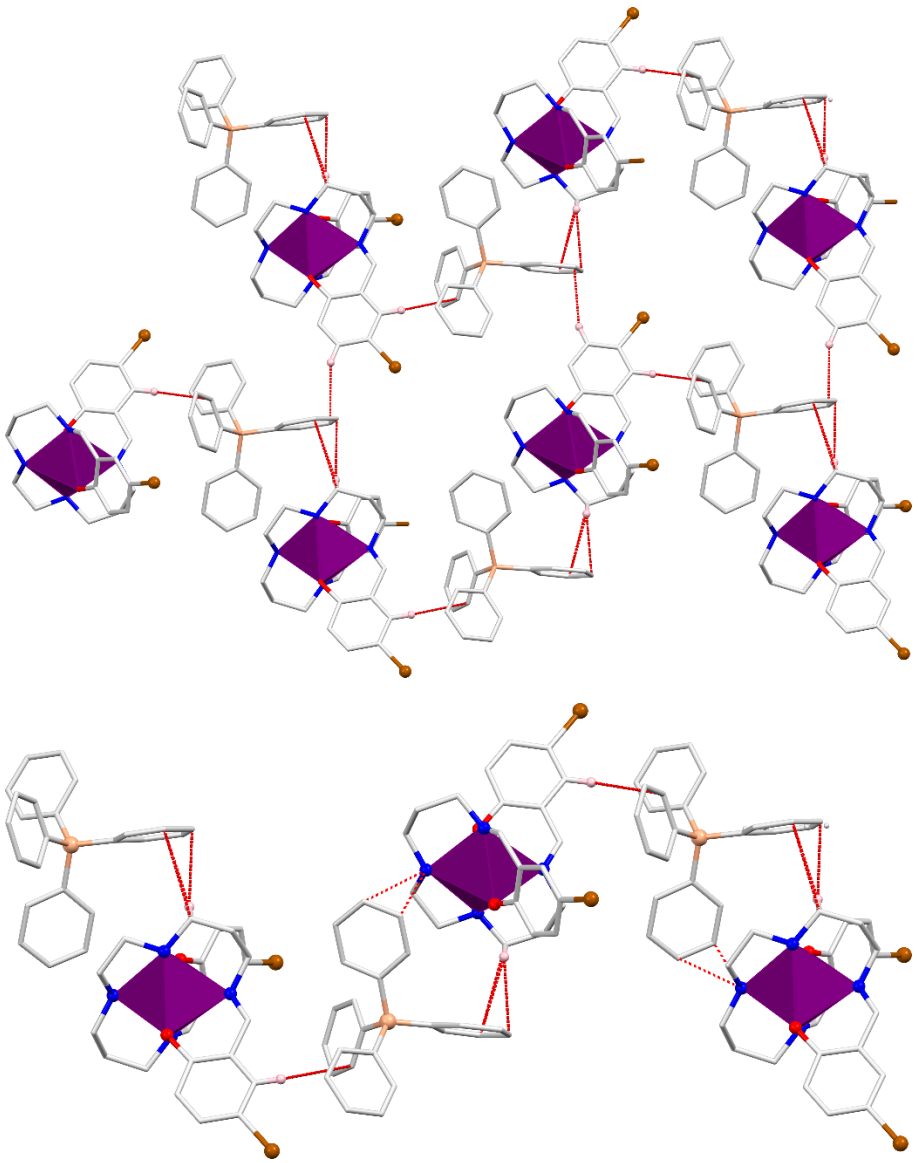

Figure S16. Top: Perspective view of a fragment of the supramolecular structure displaying several weak interactions (red lines) in **2** at 240 K. Bottom: View of N–H···C interactions forming 1D chain in **2** at 240 K.

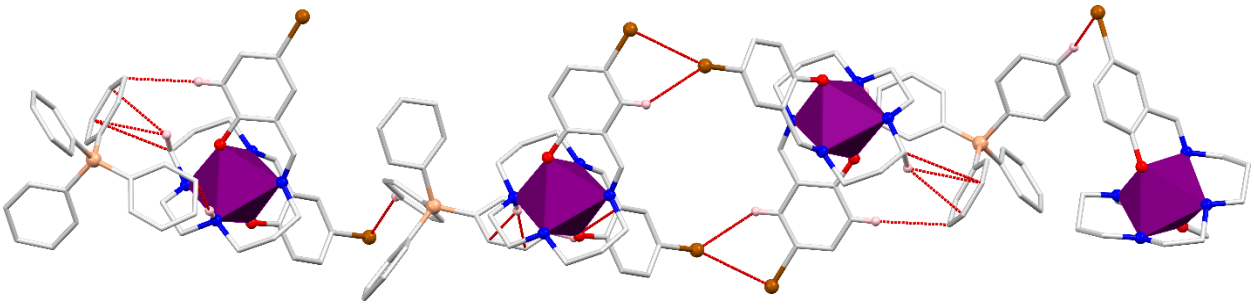

Figure S17. Top: Perspective view of a fragment of the supramolecular structure displaying several weak interactions (red lines) in **2** at 120 K.

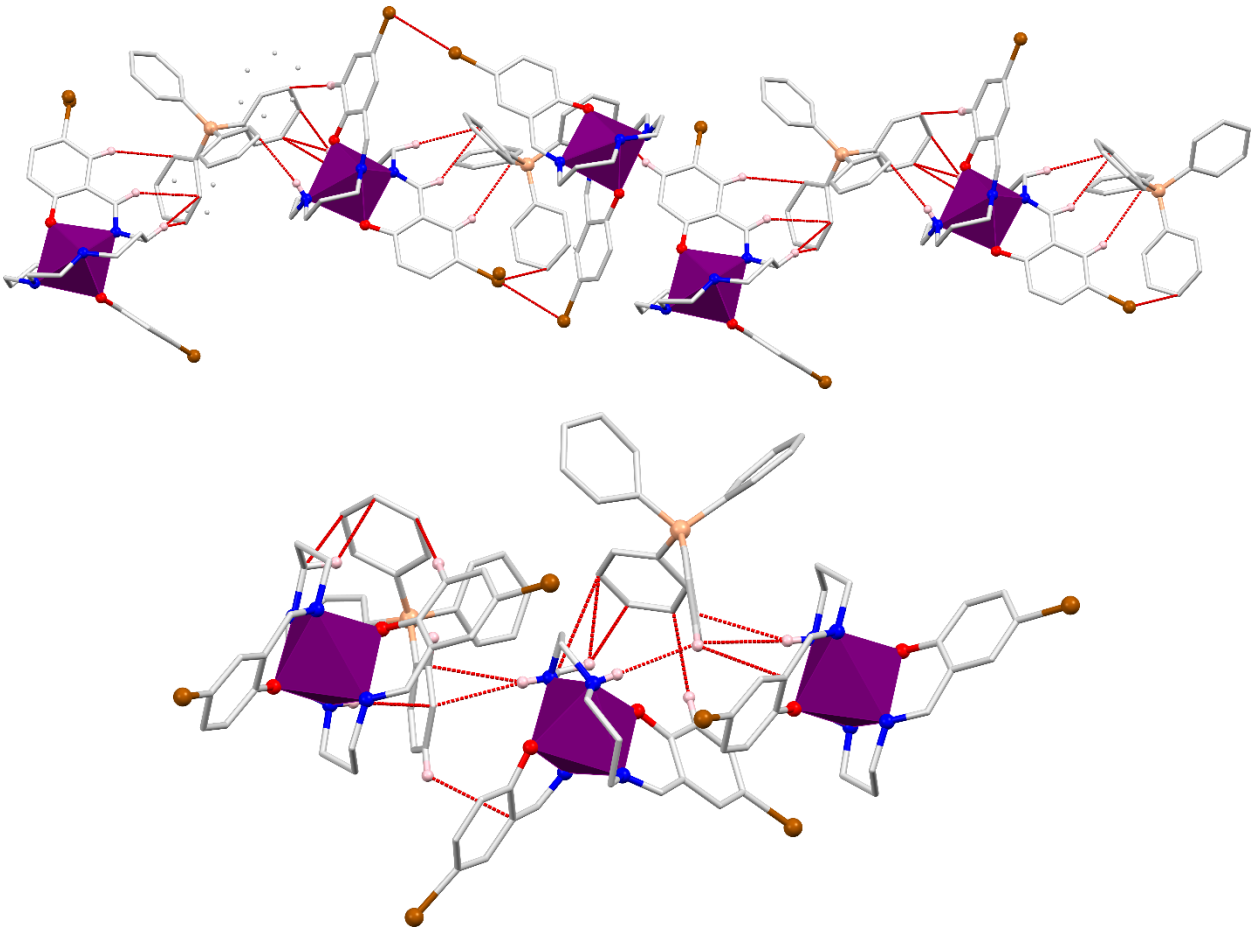

Figure S18. Perspective view of a fragment of the supramolecular structure displaying several weak interactions (red lines) in **2** at 100 K. Bottom: View of N–H···C interactions forming 1D chain in **2** at 100 K.

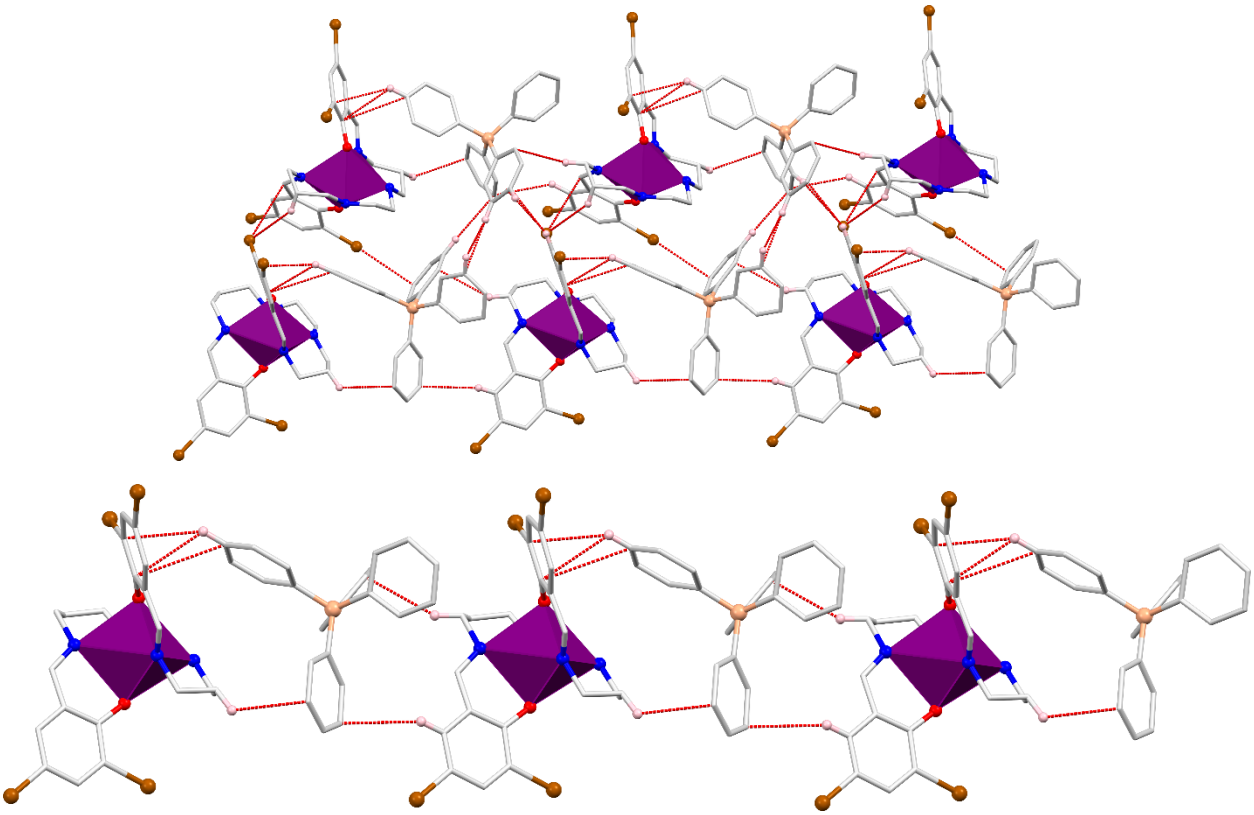

Figure S19. Top: Perspective view of a fragment of the supramolecular structure displaying several weak interactions (red lines) in **3** at 240 K. Bottom: View of N–H···C interactions forming 1D chain in **3** at 240 K.

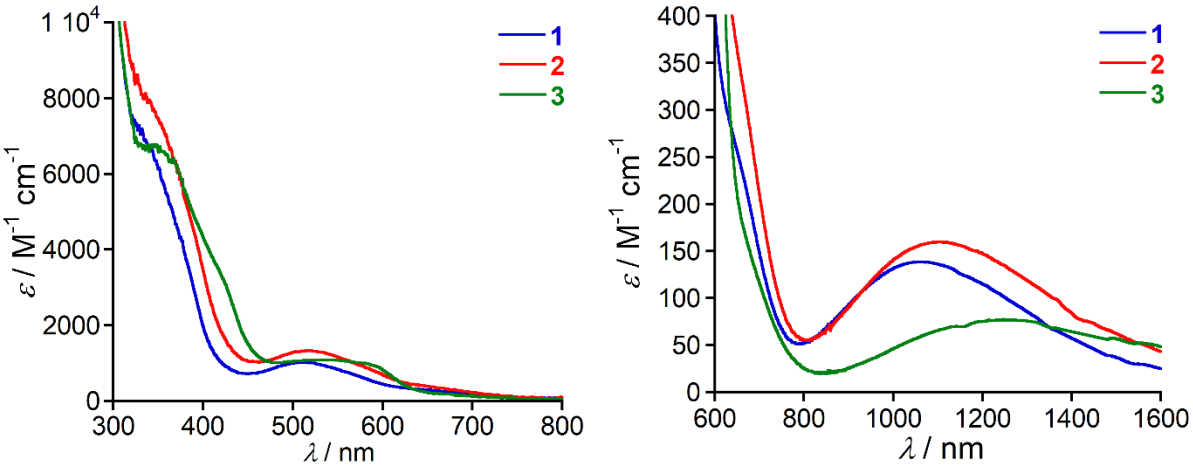

Figure S20. UV-vis-NIR spectra of **1** – **3** in MeCN with dilute (left) and concentrated (right) solutions at room temperature.

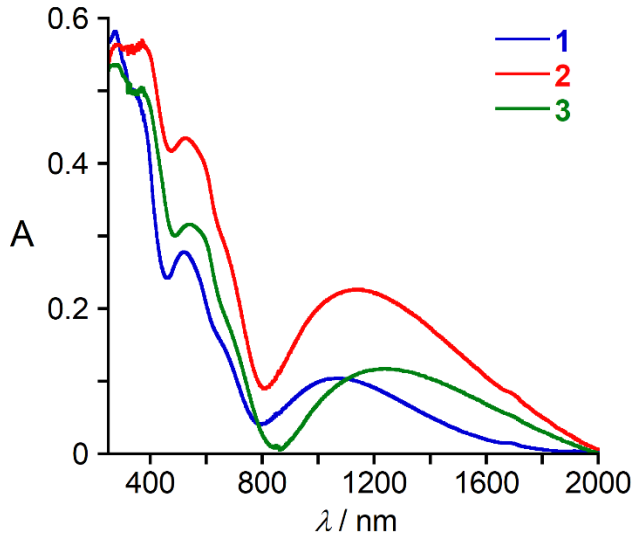

Figure S21. Solid state UV-vis-NIR spectra of **1** – **3** in KBr at room temperature.

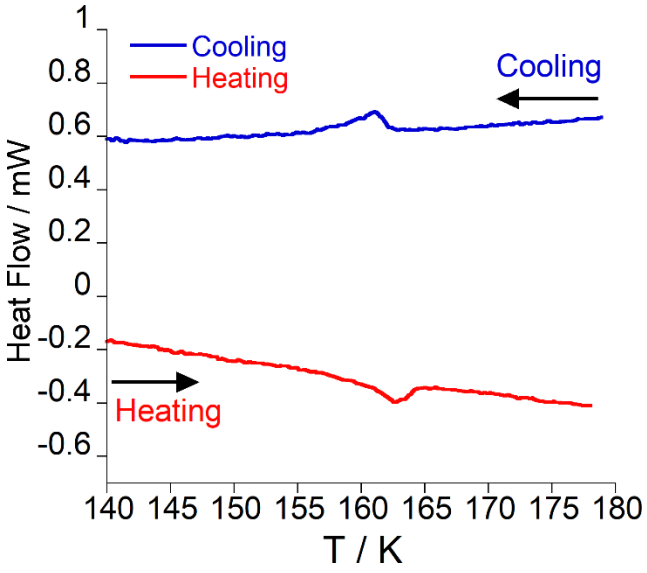

Figure S22. DSC plot of **2** shown between 180 and 140 K at a sweep rate of 5 K min^{-1}.

Note: DSC data in the low-temperature region near 100 K are not available due to the temperature limitation of our instrument.

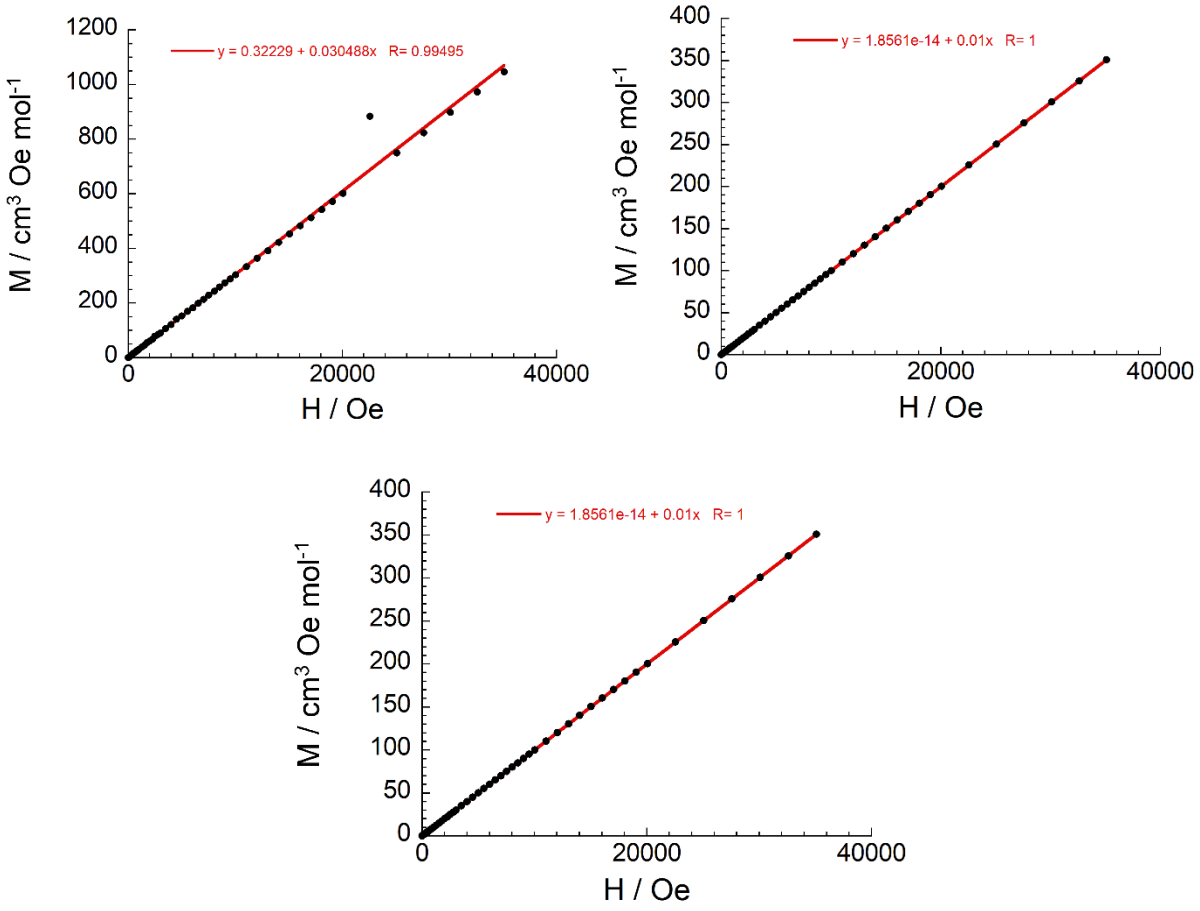

Figure S23. Field dependence of the magnetization as *M vs H* plots for **1** (Top, left), **2** (top, right) and **3** (bottom) at 100 K. The solid line is the best fit.

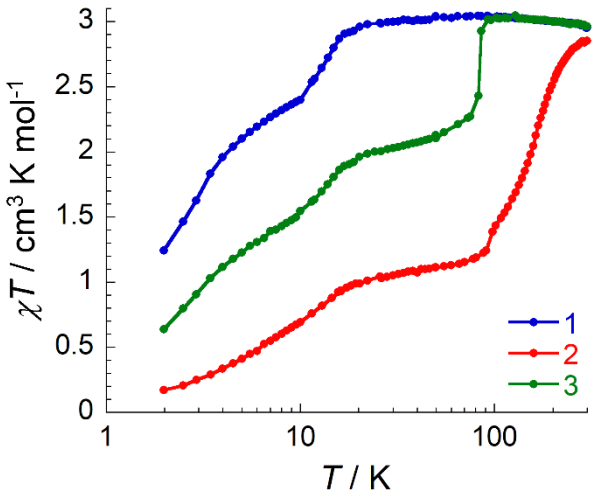

Figure S24. Temperature dependence of χT product in log scale for **1** – **3** at 10000 Oe.

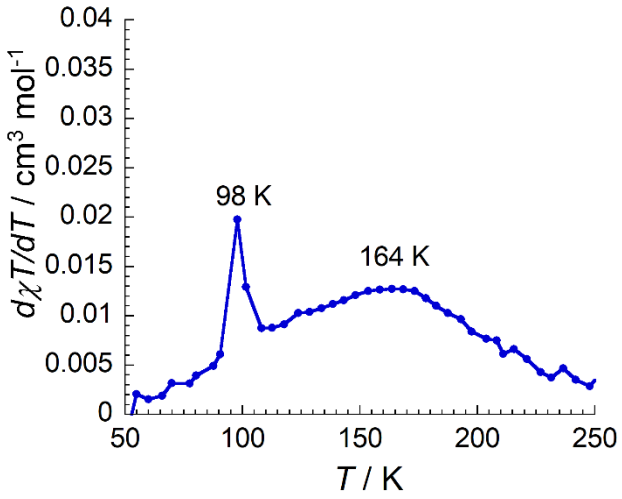

Figure S25. The first derivative of χT against the temperature, dχT /dT *vs*. T, identifies $T_{1/2}$ (1) = 164 K and $T_{1/2}$ (2) = 98 K for **2**.

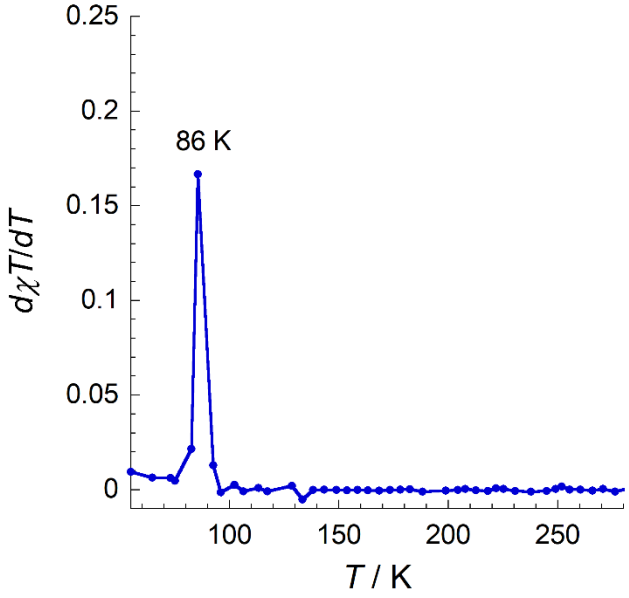

Figure S26. The first derivative of χT against the temperature, dχT /dT *vs*. T, identifies $T_{1/2}$ (1) = 86 K for **3**.

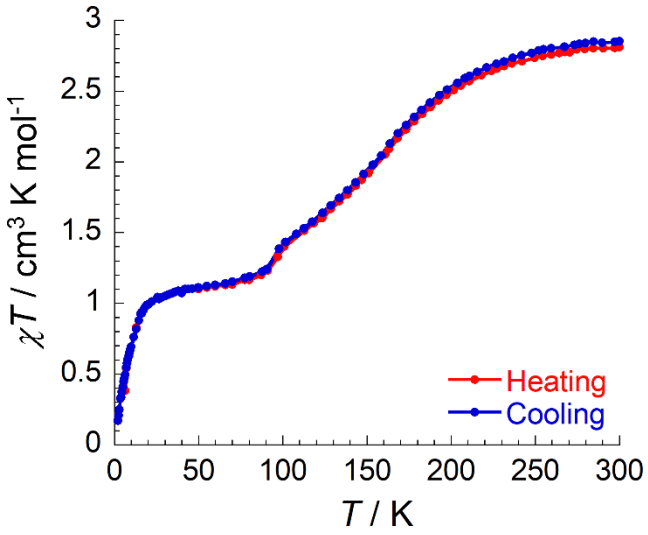

Figure S27. Temperature dependence of χT product for **2** at 10000 Oe in cooling and heating mode.

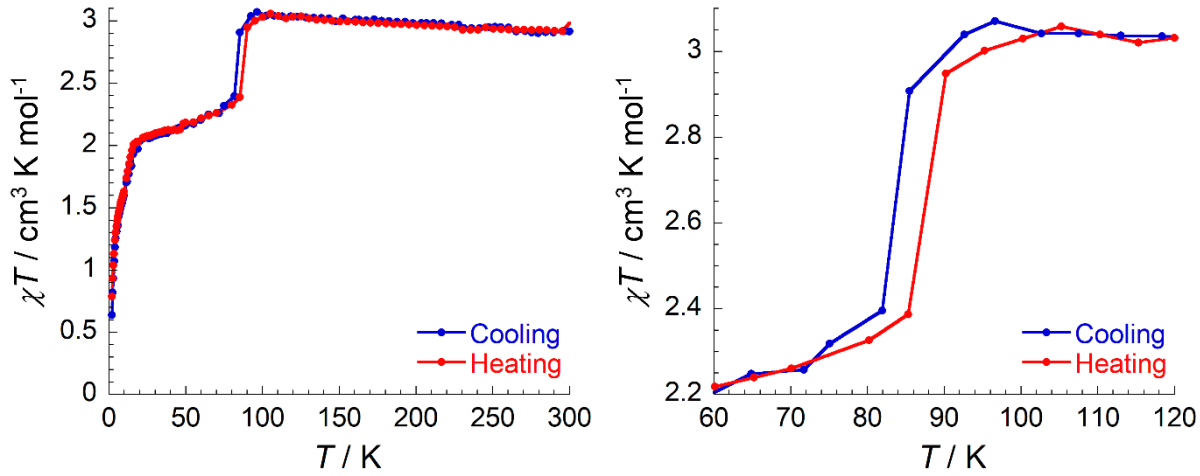

Figure S28. Left: Temperature dependence of χT product for **3** at 10000 Oe in cooling and heating mode.

Right: shown selected region (60 - 120K).

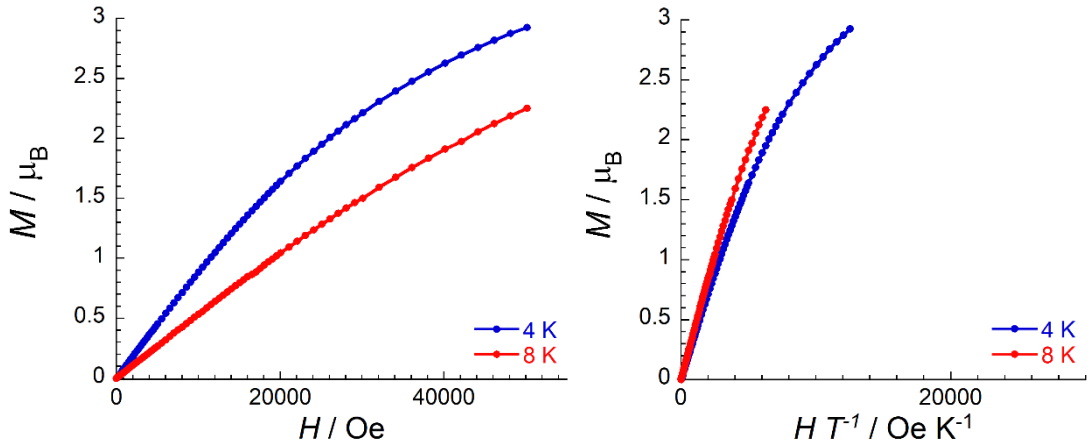

Figure S29. Field dependence of the magnetization as *M* vs *H* (left) and *M* vs *H/T* (right) plots for **1** at 4 and 8 K. The solid lines are guide for the eyes.

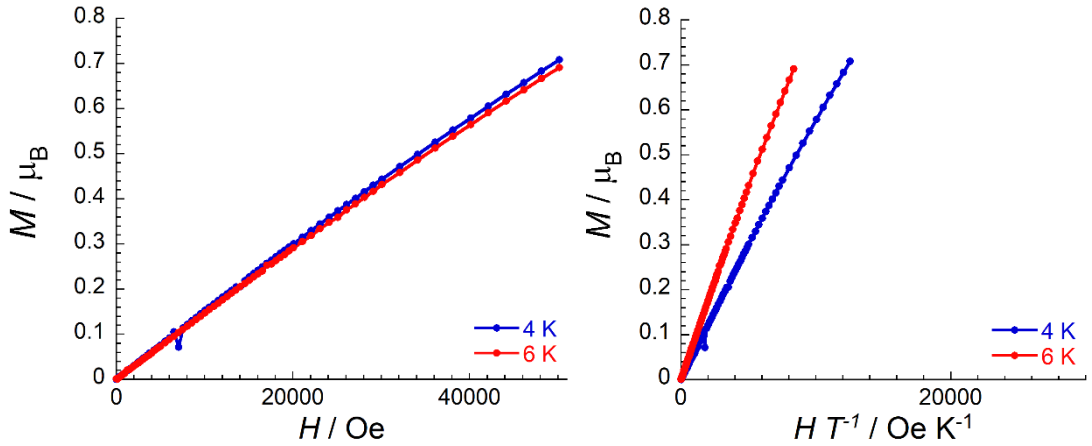

Figure S30. Field dependence of the magnetization as *M* vs *H* (left) and *M* vs *H/T* (right) plots for **2** at 4 and 6 K. The solid lines are guide for the eyes.

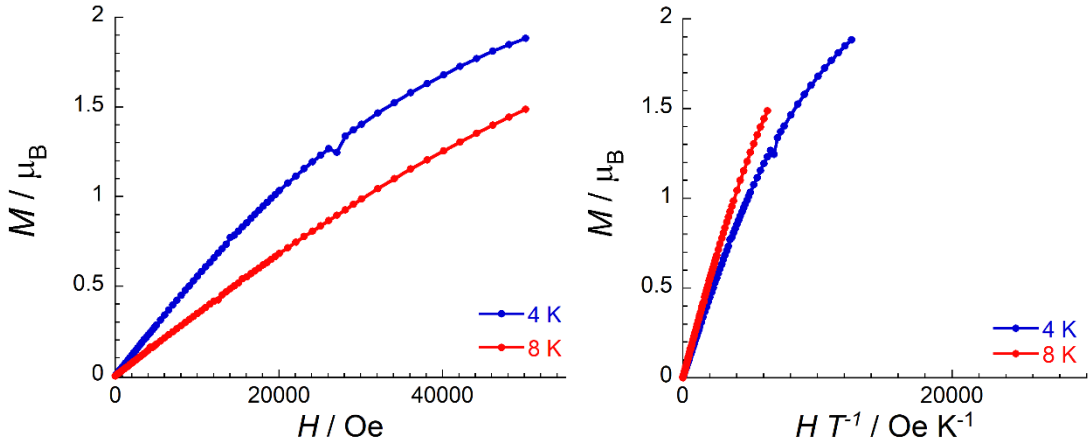

Figure S31. Field dependence of the magnetization as *M* vs *H* (left) and *M* vs *H/T* (right) plots for **3** at 4 and 8 K. The solid lines are guide for the eyes.

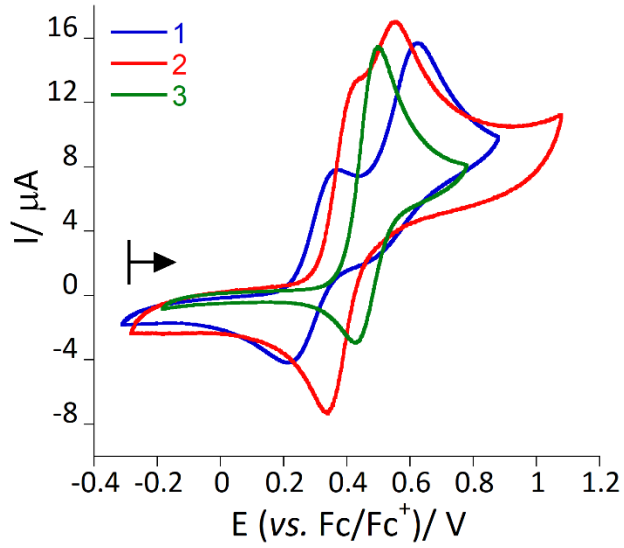

Figure S32. Cyclic voltammograms for oxidation of **1** – **3** in 0.2 M (^{n}Bu$_4$N)PF$_6$ / MeCN with a scan rate of 100 mV s^{-1}. Arrow indicates the open circuit potential with the direction of the potential sweep.

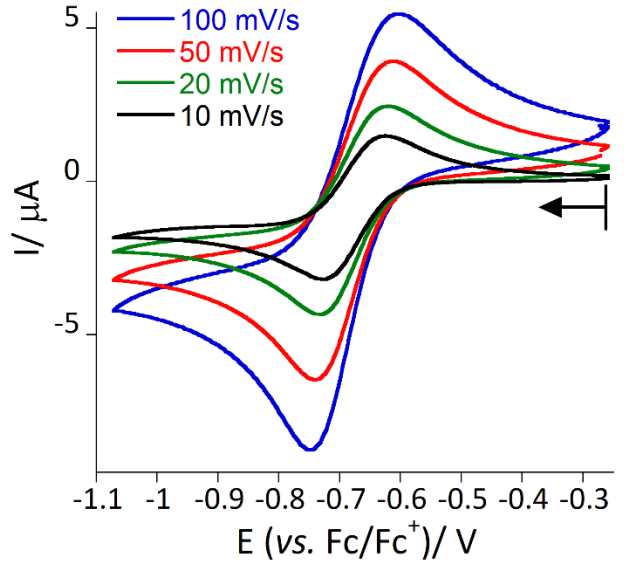

Figure S33. Cyclic voltammograms for reduction of **1** in 0.2 M (^{n}Bu$_4$N)PF$_6$ / MeCN with different scan rate. Arrow indicates the open circuit potential with the direction of the potential sweep.

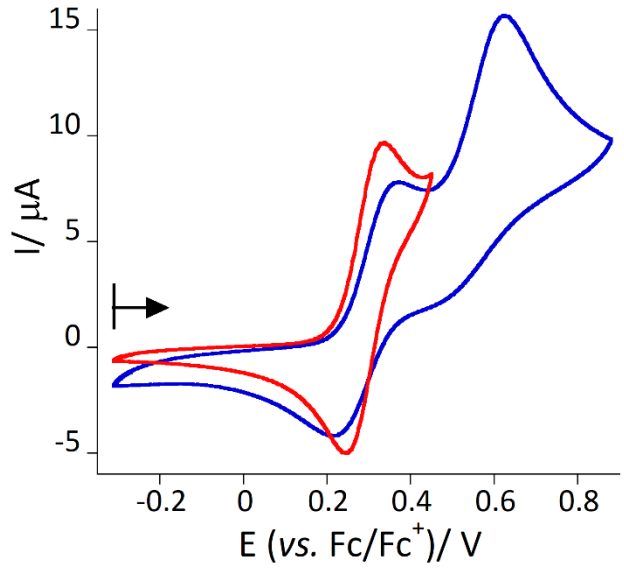

Figure S34. Cyclic voltammograms for oxidation of **1** in 0.2 M (^{n}Bu$_4$N)PF$_6$ / MeCN with a scan rate of 100 mV s^{-1}. Arrow indicates the open circuit potential with the direction of the potential sweep.

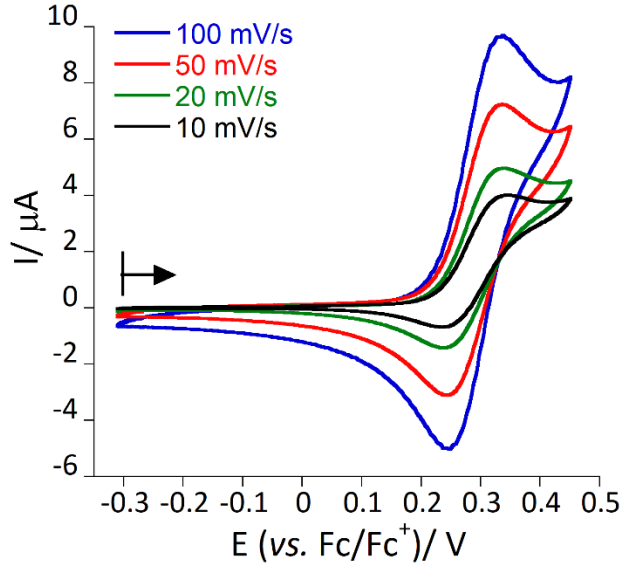

Figure S35. Cyclic voltammograms for oxidation of **1** (-0.3 V to +0.9V) in 0.2 M (^{n}Bu$_4$N)PF$_6$ / MeCN with different scan rate. Arrow indicates the open circuit potential with the direction of the potential sweep.

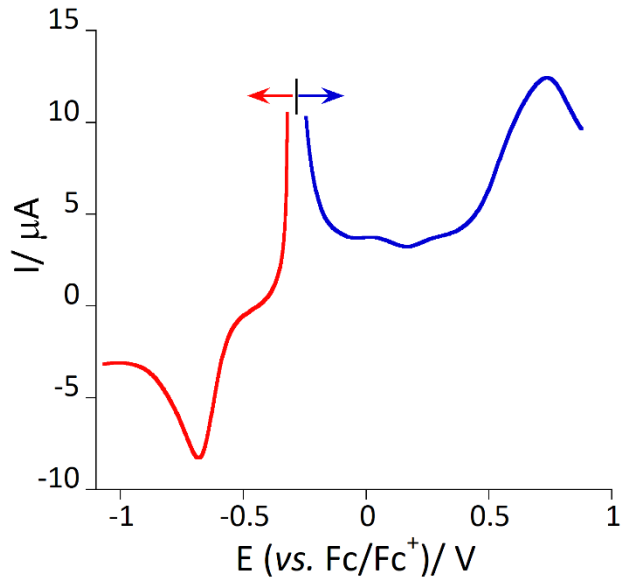

Figure S36. Square wave voltammograms for **1** in 0.2 M (^{n}Bu$_4$N)PF$_6$ / MeCN. Arrows indicate the open circuit potential with the direction of the potential sweep.

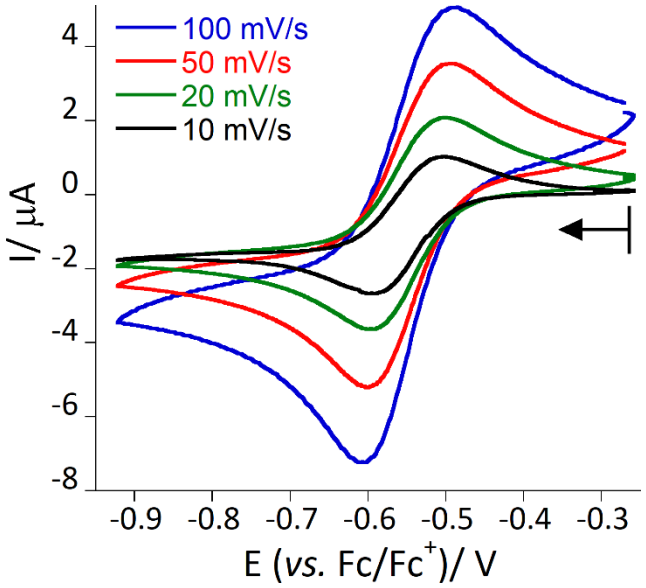

Figure S37. Cyclic voltammograms for reduction of **2** in 0.2 M (^{n}Bu$_4$N)PF$_6$ / MeCN with different scan rate. Arrow indicates the open circuit potential with the direction of the potential sweep.

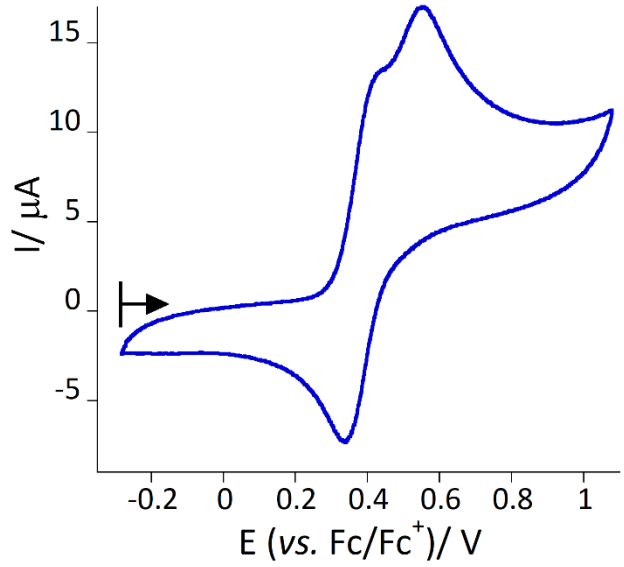

Figure S38. Cyclic voltammogram for oxidation of **2** in 0.2 M (^{n}Bu$_4$N)PF$_6$ / MeCN with a scan rate of 100 mV s^{-1}. Arrow indicates the open circuit potential with the direction of the potential sweep.

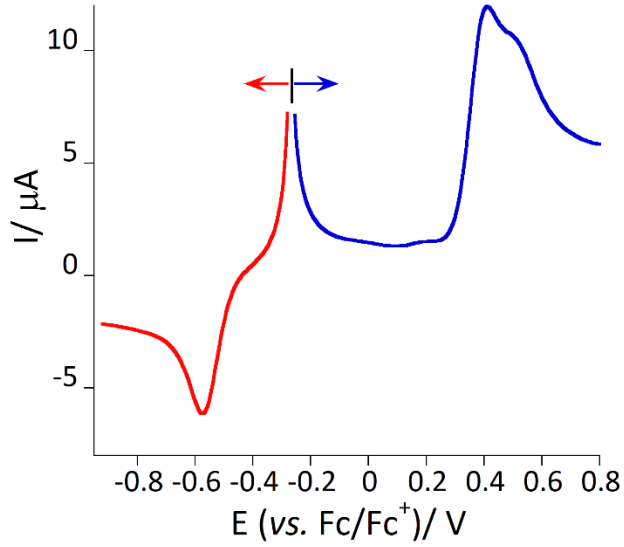

Figure S39. Square wave voltammograms for **2** in 0.2 M (^{n}Bu$_4$N)PF$_6$ / MeCN. Arrow indicates the open circuit potential with the direction of the potential sweep.

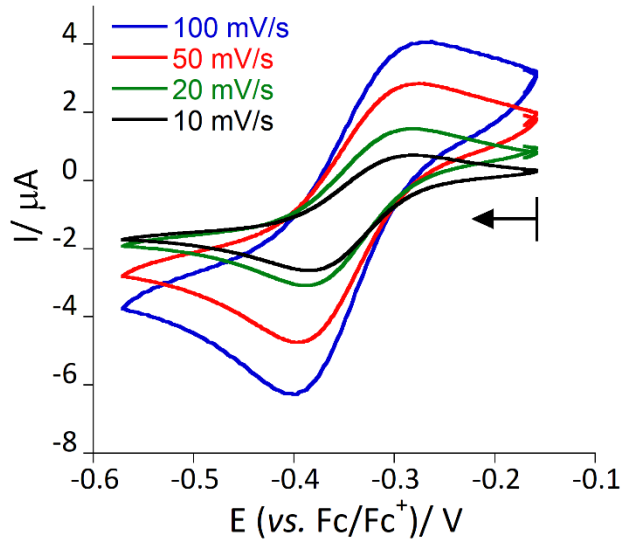

Figure S40. Cyclic voltammogram for reduction of **3** in 0.2 M (^{n}Bu$_4$N)PF$_6$ / MeCN with different scan rate. Arrow indicates the open circuit potential with the direction of the potential sweep.

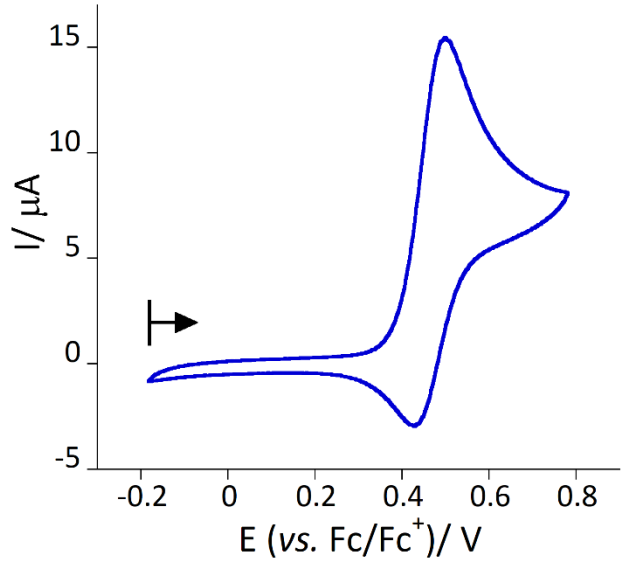

Figure S41. Cyclic voltammogram for oxidation of **3** in 0.2 M (^{n}Bu$_4$N)PF$_6$ / MeCN with a scan rate of 100 mV s^{-1}. Arrow indicates the open circuit potential with the direction of the potential sweep.

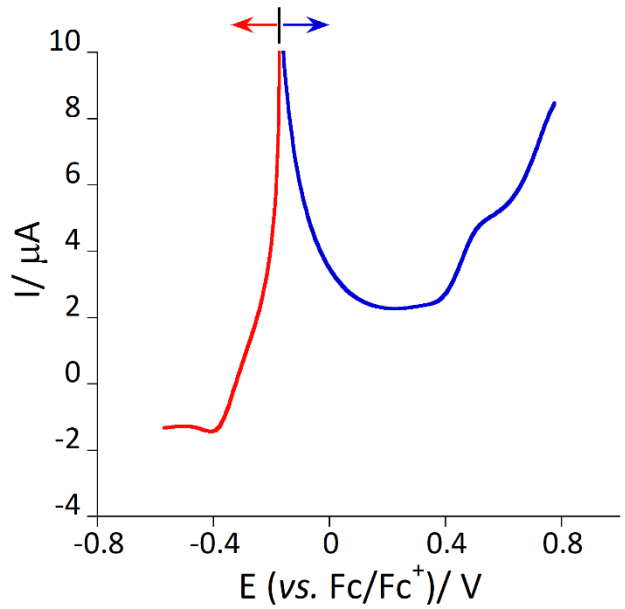

Figure S42. Square wave voltammograms for **3** in 0.2 M (^{n}Bu$_4$N)PF$_6$ / MeCN. Arrow indicates the open circuit potential with the direction of the potential sweep.

Cyclic voltammograms and square wave voltammogram of NaBPh$_4$ show an irreversible at around E_{pc}= 0.51 V *vs* Fc/Fc$^+$ (Fig. S43 and S44).

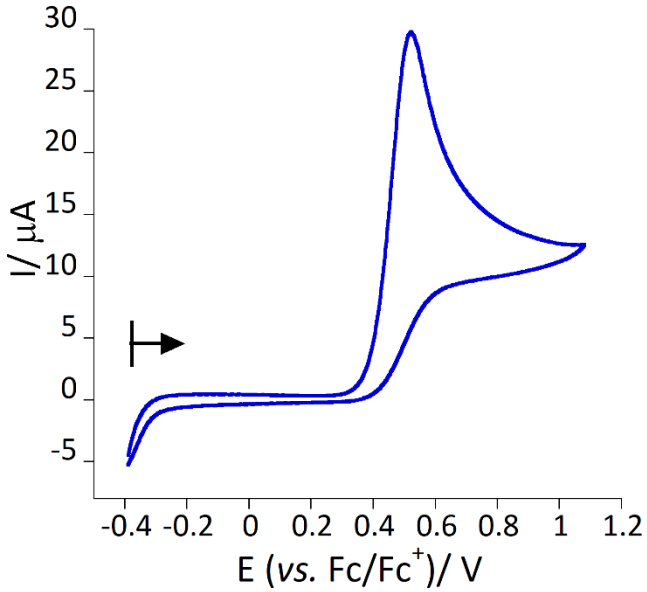

Figure S43. Cyclic voltammogram for oxidation of NaBPh$_4$ in 0.2 M (^{n}Bu$_4$N)PF$_6$ / MeCN with a scan rate of 100 mV s^{-1}. Arrow indicates the open circuit potential with the direction of the potential sweep.

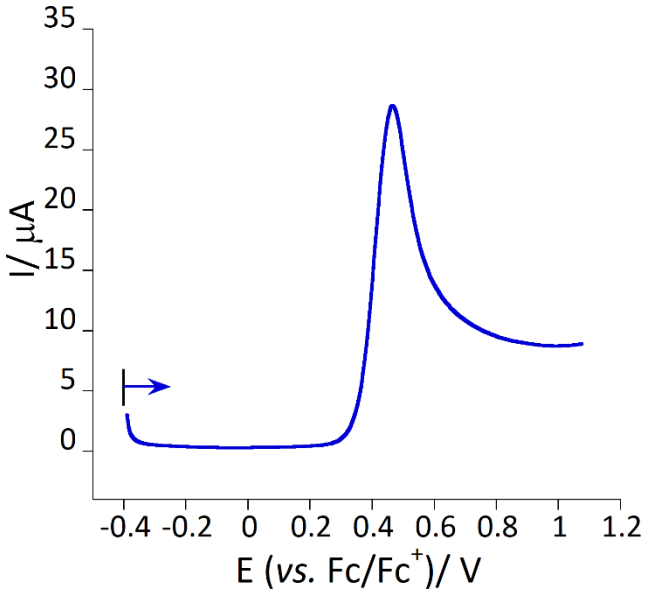

Figure S44. Square wave voltammogram for oxidation of $NaBPh_4$ in 0.2 M ($^{n}Bu_4N)PF_6$ / MeCN. Arrow indicates the open circuit potential with the direction of the potential sweep.

Tables

Table S1. X-ray crystallography data for complexes **1** – **3**.

Complex	**1**	**2**			**3**
CCDC no	2019289	2019295	2019302	2019306	2019310
temp (K)	240	240	120	100	240
empirical formula	$C_{46}H_{48}BMnN_4O_2$	$C_{46}H_{46}BBr_2MnN_4O_2$	$C_{46}H_{46}BBr_2MnN_4O_2$	$C_{46}H_{46}BBr_2MnN_4O_2$	$C_{46}H_{44}BBr_4MnN_4O_2$
formula wt	754.66	912.46	912.46	912.46	1070.25
cryst syst	Monoclinic	Monoclinic	Monoclinic	Monoclinic	Monoclinic
space group	$P2_1/n$	$P2_1/n$	$P2_1/n$	$P2_1/n$	Cc
a (Å)	11.1220(14)	14.4374(3)	14.2943(11)	14.3170(6)	14.8559(9)
b (Å)	26.211(3)	22.1423(4)	21.8580(17)	21.8581(9)	22.7886(15)
c (Å)	13.9022(18)	14.4488(3)	14.4084(12)	14.4597(6)	14.2271(9)
α (deg)	90	90	90	90	90
β (deg)	108.888(8)	115.721(1)	116.226(3)	116.332(2)	116.612(2)
γ (deg)	90	90	90	90	90
V, Å^3	3834.5(9)	4161.30(15)	4038.4(6)	4055.5(3)	4305.3(5)
Z	4	4	4	4	4
d_{calcd} (g cm^{-3})	1.307	1.448	1.492	1.468	1.649
μ (mm^{-1})	0.389	2.281	2.350	2.339	4.062
F(000)	1592	1836	1844	1800	2132
θ_{max} (deg)	30.782	30.610	30.644	30.690	30.692
completeness (%)	98.8	99.6	99.5	99.1	99.4
no. of. rflns collected	11819	12773	12413	12472	13252
no. of. Indep rflns	4531	8178	5296	7881	4978
goodness of fit on F^2	0.947	1.019	1.007	1.073	0.963
final R indices (I>2σ(I))	R1 = 0.0627 wR2 = 0.1084	R1 = 0.0440 wR2 = 0.1002	R1 = 0.0712 wR2 = 0.2012	R1 = 0.0651 wR2 = 0.1436	R1 = 0.0626 wR2 = 0.2260
final R indices (all data)	R1 = 0.2090 wR2 = 0.1502	R1 = 0.0854 wR2 = 0.1180	R1 = 0.1344 wR2 = 0.1472	R1 = 0.1160 wR2 = 0.1650	R1 = 0.1060 wR2 = 0.1485

Table S2. Selected bond distances (Å) and bond angles (°) in **1 – 3**.

Complex	**1**	**2**			**3**
	240 K	240 K	120 K	100 K	240 K
Mn(1)-N(1)	2.196(4)	2.196(2)	2.076(5)	2.074(3)	2.200(10)
Mn(1)-N(2)	2.198(3)	2.173(2)	2.081(4)	2.068(4)	2.229(10)
Mn(1)-N(3)	2.082(2)	2.103(3)	1.996(4)	1.999(4)	2.089(9)
Mn(1)-N(4)	2.084(2)	2.060(2)	2.015(4)	1.992(4)	2.059(9)
Mn(1)-O(1)	1.8558(18)	1.858(2)	1.864(3)	1.869(3)	1.860(7)
Mn(1)-O(2)	1.8620(18)	1.868(2)	1.867(3)	1.869(3)	1.858(7)
N(1)-Mn(1)-N(2)	79.74(10)	81.24(8)	83.93(18)	84.26(14)	79.5(4)
N(1)-Mn(1)-N(3)	162.32(10)	164.94(8)	170.04(18)	171.75(15)	159.3(4)
N(1)-Mn(1)-N(4)	85.46(10)	85.39(8)	88.37(18)	88.44(15)	87.1(4)
N(1)-Mn(1)-O(1)	94.89(9)	92.48(8)	84.84(16)	91.09(13)	93.8(3)
N(1)-Mn(1)-O(2)	85.30(9)	85.14(8)	91.97(16)	87.01(13)	86.2(3)
N(2)-Mn(1)-N(3)	84.79(9)	85.32(8)	88.14(17)	88.80(15)	81.3(4)
N(2)-Mn(1)-N(4)	163.38(9)	164.88(9)	170.65(18)	171.12(14)	165.7(4)
N(2)-Mn(1)-O(1)	86.46(9)	86.99(7)	91.56(16)	85.36(13)	89.4(3)
N(2)-Mn(1)-O(2)	94.21(9)	93.02(8)	86.60(15)	91.23(13)	93.7(4)
N(3)-Mn(1)-N(4)	110.89(9)	108.72(8)	100.05(17)	98.84(15)	112.6(4)
N(3)-Mn(1)-O(1)	92.63(9)	93.56(8)	89.38(15)	92.81(13)	93.5(3)
N(3)-Mn(1)-O(2)	87.37(9)	88.85(8)	93.56(15)	88.68(13)	87.6(3)
N(4)-Mn(1)-O(1)	87.33(9)	86.57(7)	93.03(16)	89.73(13)	86.6(3)
N(4)-Mn(1)-O(2)	92.04(9)	92.85(8)	88.37(15)	93.44(14)	90.3(3)
O(1)-Mn(1)-O(2)	179.33(9)	177.58(8)	176.48(16)	176.26(14)	176.9(3)

Continuous Shape Measures (CShM) Analysis:

Continuous Shape Measures (CShM) analyses were carried out to determine the geometry around Mn ion. Based on the values obtained, the idealized polyhedron was matched with the actual coordination spheres. The smallest value is symbolic of the proximity of the actual coordination sphere and idealized polyhedron.

Table S3: CShM analysis data for complexes **1** – **3**.

Complex	Temp.	Structure				
		HP - 6	PPY - 6	**OC - 6**	TPR - 6	JPPY - 6
1	240 K	31.929	23.754	**1.484**	10.842	26.477
2	240 K	32.019	24.598	**1.248**	11.503	27.391
	120 K	32.675	27.511	**0.495**	13.560	30.575
	100 K	32.803	27.956	**0.390**	14.069	31.002
3	240 K	32.148	22.826	**1.730**	10.512	25.607

HP – 6: Hexagon (D6h), PPY – 6 = Pentagonal pyramid, OC – 6: Octahedron (Oh), TPR – 6: Trigonal prism (D3h), JPPY – 6 = Johnson pentagonal pyramid J2 (C5v);

Octahedral Distortion Parameters[5]

$\sum$ is the sum of the deviation from 90° of the 12 *cis*-angles of the MnN_4O_2 octahedron; Θ is the sum of the deviation from 60° of the 24 trigonal angles of the projection of the MnN_4O_2 octahedron onto the trigonal faces; ζ is the distance distortion parameter, which is the sum of deviation from individual M-N/O bond distances with respect to the mean metal-ligand bond distance.

Table S4. Spin crossover behaviors of [Mn(X-sal$_2$-323)](BPh$_4$) (X = ligand substituent) complexes with associated Mn–N/O bond distances

Complex **X**	$T_{1/2}$ (K)[a]	T (K)[b]	Mn–O (Å)	Mn–N (Å)	Spin State	Ref.
[Mn(5H-sal$_2$-323)](BPh$_4$) **X = 5-H**	HS	240	1.8558(18)-1.8620(18)	2.082(2)-2.198(3)	HS	This work
[Mn(5Br-sal$_2$-323)](BPh$_4$) **X = 5-Br**	$T_{1/2}$ (1) = 164 K $T_{1/2}$ (2) = 98 K Two-step and complete	100 120 240	1.868(2)-1.876(2) 1.868(2)-1.875(2) 1.864(3)-1.867(3) 1.858(2)-1.868(2)	1.989(3)-2.061(3) 1.997(3)-2.077(3) 1.996(4)-2.081(4) 2.060(2)-2.196(2)	LS LS HS	This work
[Mn(3,5-Br-sal$_2$-(323))](BPh$_4$) **X = 3,5-diBr**	$T_{1/2}\downarrow$ = 86 $T_{1/2}\uparrow$ = 90 ΔT=4 K hysteretic and abrupt [HS][HS] to [HS][LS] (1:1)	240	1.858(7)-1.860(7)	2.059(9)-2.229(10)	HS	This work
[Mn(5Cl-sal$_2$-323)](BPh$_4$) **X = 5-Cl**	$T_{1/2}$ (1) = 168 K $T_{1/2}$ (2) = 103 K Two-step and complete	100 120 240	1.8753(13)-1.8661(13) 1.856(4)-1.864(4) 1.865(4)-1.861(4) 1.8650(19)-1.8540(19)	2.0742(18)-2.0808(16) 2.0005(17)-2.0085(17) 2.139(5)-2.121(5) 2.047(5)2.022(5) 2.098(5)-2.101(5) 2.005(5)-2.018(5) 2.167(3)-2.179(3) 2.060(2)-2.095(3)	LS HS]:[LS] (1:1) HS	[6]
[Mn(3-OEt-sal$_2$-323)](BPh$_4$) **X = 3-OEt**	HS	100	1.8687(10)-1.8586(10)	2.0950(11)-2.2479(12)	HS	[7]
[Mn(3-OMe-sal$_2$-323)](BPh$_4$) **X = 3-OMe**	HS	100	1.8516(18)-1.8829(18)	2.065(2)–2.256(2)	HS	[7]

a: spin crossover temperature; b: structure analyses temperature

Table S5: Spin crossover behaviors of [Mn(5H-sal$_2$-323)](Y) (Y = counter anion) complexes with associated Mn–N/O bond distances

Complex X	$T_{1/2}$ (K)[a]	T (K)[b]	Mn–O (Å)	Mn–N (Å)	Spin State	Ref.
[Mn(5H-sal$_2$-323)](BPh$_4$) **Y = BPh$_4$**	HS	240	1.8558(18)-1.8620(18)	2.082(2)-2.198(3)	HS	This work
[Mn(5H-sal$_2$-323)]SbF$_6$ **Y = SbF$_6$**	HS	100 295	1.8614(10) 1.855(2)	2.1139(12)–2.2350(13) 2.107(3)–2.236(3)	HS HS	[8]
[Mn(5H-sal$_2$-323)]PF$_6$ **Y = PF$_6$**	132–134, $\Delta T_{1/2}$ = 8 Abrupt and hysteretic.	100 126 ↑ 126 ↓ 142	1.8773(14)–1.8836(14) 1.8763(15)–1.8783(16) 1.8702(12)–1.8723(12) 1.8745(19)–1.873(2)	1.9899(17)–2.0677(17) 1.9971(18)–2.0827(19) 2.0834(15)–2.2135(17) 2.086(2)–2.210(3)	LS LS HS HS	[9]
[Mn(5H-sal$_2$-323)]AsF$_6$ **Y = AsF$_6$**	$T_{1/2}$ ↓ = 146 $T_{1/2}$ ↑ = 164, $\Delta T_{1/2}$ = 18. Hysteretic, relatively abrupt	110 146 ↓ 164 ↑ 295	1.880(3)–1.878(3) 1.873(3)–1.878(3) 1.870(5)–1.873(4) 1.854(5)–1.864(5)	1.992(4)–2.068(4) 2.006(3)–2.085(4) 2.007(5)–2.123(6) 2.098(6)–2.240(7)	LS LS LS HS	[8]
[Mn(5H-sal$_2$-323)]NO$_3$·EtOH **Y = NO$_3$**	~ 290. Gradual and incomplete	100 295	1.8811(8)–1.8849(8) 1.876(2)–1.877(2)	2.0231(10)–2.1570(11) 2.049(3)–2.204(3)	LS HS	[8]
[Mn(5H-sal$_2$-323)]Cl **Y = Cl**	~315	100 295	1.877(2) 1.8712(19)	1.985(3)–2.049(3) 2.022(3)–2.097(3)	LS HS	[8]

a: spin crossover temperature; b: structure analyses temperature

Table S6: Spin crossover behaviors of [Mn(5Br-sal$_2$-323)](Y) (Y = counteranion) complexes with associated Mn–N/O bond distances

Complex X	$T_{1/2}$ (K)[a]	T (K)[b]	Mn–O (Å)	Mn–N (Å)	Spin State	Ref.
[Mn(5Br-sal$_2$-323)](BPh$_4$) **Y = BPh$_4$**	$T_{1/2}$ (1) = 164 K $T_{1/2}$ (2) = 98 K Two-step and complete	100 120 240	1.868(2)-1.876(2) 1.868(2)-1.875(2) 1.864(3)-1.867(3) 1.858(2)-1.868(2)	1.989(3)-2.061(3) 1.997(3)-2.077(3) 1.996(4)-2.081(4) 2.060(2)-2.196(2)	LS LS HS	This work
[Mn(5Br-sal$_2$-323)]NO$_3$ **Y = NO$_3$**	HS	293	1.870(2)–1.875(2)	2.078(3)–2.243(3)	HS	[10]
[Mn(5Br-sal$_2$-323)]PF$_6$ **Y = PF$_6$**	HS	293	1.866(3)–1.878(3)	2.091(3)–2.252(4)	HS	[10]
[Mn(5Br-sal$_2$-323)]TCNQ$_{1.5}$·2MeCN **Y = TCNQ$_{1.5}$**	HS	100	1.871(4)–1.886(4)	2.095(5)–2.175(5)	HS	[11]
[Mn(5Br-sal$_2$-323)]ClO$_4$ **Y = ClO$_4$**	~ 175. Gradual [HS][HS] to [HS][LS] (1:1)	100 294	1.867 1.881 1.865(3)–1.869(3)	2.110–2.200 1.999–2.060 2.086(4)–2.184(4)	HS HS	[12]

a: spin crossover temperature; b: structure analyses temperature

Table S7: Spin crossover behaviors of [Mn(3,5Br-sal$_2$-323)](Y) (Y = counter anion) complexes with associated Mn–N/O bond distances

Complex X	$T_{1/2}$ (K)[a]	T (K)[b]	Mn–O (Å)	Mn–N (Å)	Spin State	Ref.
[Mn(3,5Br-sal$_2$(323))](BPh$_4$) **Y = BPh$_4$**	$T_{1/2}\downarrow$ = 86 $T_{1/2}\uparrow$ = 90 ΔT=4 K hysteretic and abrupt [HS][HS] to [HS][LS] (1:1)	240	1.858(7)-1.860(7)	2.059(9)-2.229(10)	HS	This work
[Mn^{III}(3,5Br-sal$_2$-323)]ClO$_4$·½MeCN **Y = ClO$_4$**	75 Gradual and incomplete	100 200	1.873(2)–1.877(2) 1.869(2)–1.874(2)	1.984(3)–2.054(3) 2.024(3)–2.114(3)	LS LS	13
[Mn^{III}(3,5Br-sal$_2$-323)]BF$_4$·EtOH **Y = BF$_4$**	~175. Gradual and incomplete	100 293	1.879(3)–1.887(3) 1.869(4)–1.881(4)	1.997(5)–2.066(4) 2.053(6)–2.179(5)	LS HS	13
[Mn^{III}(3,5Br-sal$_2$-323)]CF$_3$SO$_3$·EtOH **Y = CF$_3$SO$_3$**	~ 200. Gradual and incomplete	100 293	1.8881(10)–1.8934(10) 1.881(2)–1.880(3)	1.9863(12)–2.0569(12) 2.053(3)–2.166(4)	LS HS	13
[Mn^{III}(3,5Br-sal$_2$-323)]ClO$_4$·EtOH **Y = ClO$_4$**	>200. Gradual and incomplete	100 293	1.870(4)–1.8888(4) 1.868(3)–1.882(3)	2.0009(5)–2.098(5) 2.063(5)–2.200(4)	LS HS	13
[Mn^{III}(3,5Br-sal$_2$-323)]NO$_3$·EtOH **Y = NO$_3$**	>250. Gradual and incomplete	100	1.8820(16)–1.8831(16)	1.982(2)–2.045(2)	LS	13
[Mn^{III}(3,5Br-sal$_2$-323)]PF$_6$ ½·MeOH **Y = PF$_6$**	LS	100	1.861(2)–1.879(2)	1.980(3)–2.058(3)	LS	13

a: spin crossover temperature; b: structure analyses temperature;

References

1. T. Degen, M. Sadki, E. Bron, U. König and G. Nénert, *Powder Diffr.*, 2014, **29**, S13-S18.
2. G. M. Sheldrick, SADABS Version 2.03, Bruker Analytical X-Ray Systems, Madison, WI, USA, 2000.
3. G. Sheldrick, *Acta Crystallogr., Sect. C: Struct. Chem*, 2015, **71**, 3-8.
4. L. Farrugia, *J. Appl. Crystallogr.*, 1999, **32**, 837-838.
5. R. Ketkaew, Y. Tantirungrotechai, P. Harding, G. Chastanet, P. Guionneau, M. Marchivie and D. J. Harding, *Dalton Trans.*, 2021, **50**, 1086-1096.
6. S. Ghosh, S. Bagchi, M. Das, S. Kamilya and A. Mondal, *Dalton Trans.*, 2020, **49**, 14776-14780.
7. B. Gildea, M. M. Harris, L. C. Gavin, C. A. Murray, Y. Ortin, H. Muller-Bunz, C. J. Harding, Y. Lan, A. K. Powell and G. G. Morgan, *Inorg. Chem.*, 2014, **53**, 6022-6033.
8. S. Wang, Y. J. Li, F. F. Ju, W. T. Xu, K. Kagesawa, Y. H. Li, M. Yamashita and W. Huang, *Dalton Trans*, 2017, **46**, 11063-11077.
9. P. N. Martinho, B. Gildea, M. M. Harris, T. Lemma, A. D. Naik, H. Muller-Bunz, T. E. Keyes, Y. Garcia and G. G. Morgan, *Angew. Chem., Int. Ed.*, 2012, **51**, 12597-12601.
10. B. Gildea, L. C. Gavin, C. A. Murray, H. Müller-Bunz, C. J. Harding and G. G. Morgan, *Supramol. Chem.*, 2012, **24**, 641-653.
11. A. V. Kazakova, A. V. Tiunova, D. V. Korchagin, G. V. Shilov, E. B. Yagubskii, V. N. Zverev, S. C. Yang, J. Y. Lin, J. F. Lee, O. V. Maximova and A. N. Vasiliev, *Chem. Eur. J.*, 2019, **25**, 10204-10213.
12. S. Wang, M. Ferbinteanu, C. Marinescu, A. Dobrinescu, Q. D. Ling and W. Huang, *Inorg. Chem.*, 2010, **49**, 9839-9851.
13. K. Pandurangan, B. Gildea, C. Murray, C. J. Harding, H. Muller-Bunz and G. G. Morgan, *Chem. Eur. J.*, 2012, **18**, 2021-2029.